Materials & Design 209 (2021) 109960

Contents lists available at ScienceDirect

Materials & Design

journal homepage: www.elsevier.com/locate/matdes

How would the deformation bands affect recrystallization in pure aluminium?

Qinmeng Luan [a], Jianglong Wang [a], Yan Huang [b], Daniel S. Balint [a], Jun Jiang [a,*]

[a] Department of Mechanical Engineering, Imperial College London, London SW7 2AZ, UK
[b] BCAST, Brunel University, Uxbridge, Middlesex UB8 3PH, UK

HIGHLIGHTS

- The initial grain nucleation prefers to occur inside of the DBs in the comparison with grain boundaries.
- DB is demonstrated to be the source of orientations and positions for the nucleated grains.
- The area fraction of DBs has a positive correlation with the number of nucleated grains which would contribute to the RX rate.
- The developed KWC phase-field model successfully calculated the kinetics of the RX process in different microstructures.

GRAPHICAL ABSTRACT

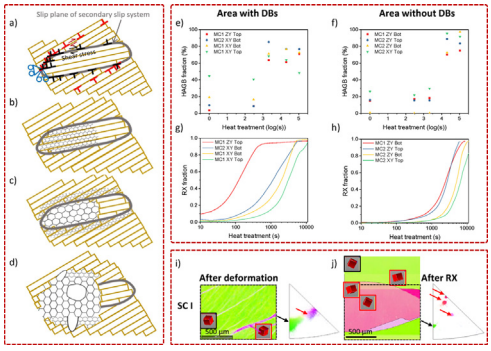

ARTICLE INFO

Article history:
Received 8 April 2021
Revised 20 June 2021
Accepted 4 July 2021
Available online 10 July 2021

Keywords:
Deformation band
Grain nucleation
Grain growth
Phase-field model
Recrystallization

ABSTRACT

Deformation bands (DBs), formed after plastic deformation, are known to have an impact on the recrystallization (RX) process. The exact mechanisms of how DBs influence grain nucleation and grain growth remain unclear. In this paper, deformed single and multicrystal pure aluminium samples are annealed to explore the likely effects of DBs on the grain nucleation and the subsequent grain growth. Regarding the prediction of the recrystallized (RXed) texture, it is noticeable that the orientations of nucleated grains nearby DB are originated from the orientation in DB. Regarding the nucleated positions, it is demonstrated that potential nucleation sites are more likely located in DBs in comparison with the initial grain boundary. Regarding the rate of RX, the number of nucleated grains is also predicted to have a strong positive correlation with the area fraction of DBs, which would consequently affect the kinetics of the grain growth in the deformed microstructure. All the above observations imply that the RX process is strongly controlled by the ensemble characteristics of DBs rather than the initial grain boundaries.

1. Introduction

The term recrystallization (RX) defined by Doherty, Gottstein, Hirsch et al. [2] in 1988, describes the formation of a new grain structure in the deformed material by the formation and migration of high angle grain boundaries (HAGBs). Microstructure control through RX, such as grain refinement and grain size homogenization, is of primary interest in metal processing to provide components with high strength, high toughness and good fatigue resistance. Hence, understanding, predicting and manipulating the RX are important in material design and manufacturing [3].

Most of the developed theories about the RX only focus on qualitatively explaining the nucleation mechanism, without further quantitative discussions on how the deformed structure affects the grain nucleation and the consequent grain growth [4]. For

* Corresponding author.
E-mail address: jun.jiang@imperial.ac.uk (J. Jiang).

https://doi.org/10.1016/j.matdes.2021.109960

example, previous work focuses on discussing the general effect of various factors, e.g. strain level, grain boundary and initial grain size, on the occurrence of grain nucleation [5]. Although the analysis on nucleated orientations [6,7] and the nucleation conditions [8-10] start to attract some interests nowadays, the quantitative criteria still need further rigorous examinations. This missing brick in the wall of RX study directly hinders the understanding of RX process as well as its simulations, especially for the prediction of recrystallized (RXed) texture and RXed grain size.

In the previous modelling work, the criteria normally used to predict grain nucleation oversimplify the processes involved, and as a result, do not match experimental findings [11-13]. For instance, the simulated nucleation sites usually are randomly chosen among the grit nodes [14], and the orientations of the nucleated grains are generally allocated by a stochastic process [14-18] which neither include the information of dislocation structure nor consider the orientation relationship between the nucleated and the initial grains. Apart from this, some recent work has tried to include the dislocation structure and the misorientation relationship into the modelling but still lack experimental support for the assignment of the nucleated grains [18,19]. Consequently, current RX models have limited manufacturing usage due to the unknown relation between dislocation structure and RX.

Therefore, it is essential to understand how the grain nucleates based on the heterogeneous deformed microstructure at the grain level through experiments, since nucleated positions, nucleated orientations and the number of nucleated grains are all determined at this stage for the RX process [5,13,18,20,21]. The heterogeneities in the deformed metal are generally caused by a slip, slip band, deformation band and shear band [2] (see Fig. 1).

Slip is a primary deformation mechanism for cubic metals. Slip bands are localized aggregate of parallel slip in individual grains whose orientation is affected by the grain orientation. Thus, slip bands cannot cross the grain boundary [22]. As a result, slip bands can create high plastic strain and cannot create localised orientation changes during plastic deformation.

The term deformation band (DB) was defined by Barrett et al. [23] in 1939, describing a volume of approximately constant orientation that is significantly different to the orientation elsewhere in that grain. It was demonstrated by the Digital Image Correlation (DIC) technique that strains were concentrated in DBs, giving rise to orientation gradients and eventual fragmentation of grains [2]. Therefore, like the slip band, DB is determined by the crystallographic nature and contains a high level of strain [2]. However, unlike the slip band, DB is relevant to generating a volume of new constant orientation.

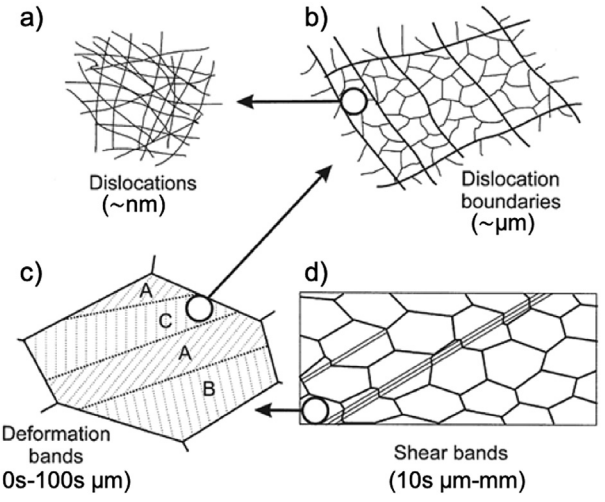

Fig. 1. The various features in a deformed polycrystalline metal at increasing scale: a) dislocations; b) dislocation boundaries; c) deformation and transition bands within a grain; d) specimen and grain-scale shear bands [2].

Shear bands are characterised by non-crystallographic bandlike narrow regions of highly concentrated flow across many grains, while the abutting matrix undergoes comparably low and homogeneous plastic flow [24]. Shear bands can provide extensive amounts of dislocations and orientation gradients for RX occurrence [2]. Therefore, intensive shear is always required for the creation of shear bands. Also, the deformed texture and RXed texture caused by shear bands are widely studied [2]. Therefore, this work focus on the effect of DBs on recrystallization.

In plastically deformed alloys [5], a larger number of deformation bands (DBs), that can effectively accommodate the plastic strain and give rise to the heterogeneities in microstructure, are observed and well explained in our previous work [25]. Furthermore, a higher magnitude of dislocation density is found near the grain boundaries due to the prohibition of dislocation transmission from the neighbouring grain [26,27]. Hence, both DBs and grain boundaries could be the possible nucleated sites for RX [2,18].

DBs are found in various alloys, such as steel [28], zinc [29], aluminium [7], copper [30], nickel [31], magnesium [32], titanium [33] and etc. in both single crystal and polycrystalline structure. Therefore, understanding the formation of DBs by examining their crystallographic features is crucial to understand the RX process in engineering alloys regarding grain nucleation, grain growth, and simulation, especially for the nucleation criteria and nucleated grain orientations. However, there are long-standing problems remaining unclear which greatly hinder the construction of RX models for the quantitative prediction and manipulation of the microstructural evolution. For example, how does the DB compete with other microstructure features, such as grain boundaries, triple junctions, on the accumulation of dislocation density for the grain nucleation process? Is the DBs the dominating factor for the RX process? How does the DB quantitatively control the evolution rate of texture and microstructure? All the above questions are going to be discussed in this work.

Through combining the microstructural characterization and phase-field modelling, this work aims to quantitatively address this crucial problem by analysing: the effect of orientations in DBs on the RXed texture formation; the competition between DBs and grain boundaries on the nucleation sites; the effect of DBs on the rate of RX process. The comprehensive quasi-in-situ electron back-scattered diffraction (EBSD) study on the evolution of grain orientation would provide insights into this problem. Initially, the experimental observations on the grain nucleation regarding nucleated positions and nucleated orientations can be written as nucleation laws in the Kobayashi, Warren and Carter (KWC) phase-field model. Furthermore, the experimental EBSD results for the RX process are capable of validating the simulated RX kinetics by KWC phase-field model.

In this work, the simplest and most studied materials, high purity aluminium, were carefully chosen in this work to add the quantitative analysis of the effect of DBs on RX for the previous work. The high purity Al work also completed the story of how DBs are formed and then control the RX in addition to our previous paper about the formation of DBs [25]. The deformed multicrystals and single crystals of pure aluminium were heat-treated at 450 °C for different times to capture and predict the whole RX process in three dimensions (3D) with the aid of quasi-in-situ EBSD technique and KWC phase-field modelling. The experimentally observed and phase-field simulated grain nucleation and the subsequent grain growth are explained in as a unified manner.

2. Experiments and phase-field model

2.1. Materials preparation

This work used two types of uniaxial compressed pure aluminium to study the RX: one is $2 \times 2 \times 3.5$ mm^3 cuboid columnar multi-crystals (MC) with > 99.9% purity; the other one is $10 \times 10 \times 10$ mm^3 cubic single crystals (SC) with > 99.999% purity. The Czochralski technique [1] was used to get the SC and MC specimens. The grain boundaries in the MC specimens are much more stable than the grain boundaries in the conventional polycrystalline alloy. Therefore, it is hard to nucleate grains at those initial grain boundaries and cross them during grain growth. The geometries of the SC and MC samples are shown in Fig. 2 and Fig. 4. The orientations of SC and MC samples before and after deformation are shown in Fig. 3 and Fig. 4.

MC samples were uniaxially compressed to 20% and 30% engineering strain respectively; SC samples with four different orientations (i.e. SC I, II, III and IV) were compressed to 30% engineering strain. The initial orientations of SC I, II, III and IV and its orientations after deformation are shown in Fig. 4.

All compression tests were carried out using an Instron mechanical testing machine at a 0.002 s^{-1} strain rate and room temperature. Samples were lubricated by the highly stable lithium complex grease on the top and bottom sides to reduce the friction during the compression (see [25] for more details of compression tests).

The interrupted heat treatments for the deformed samples were carried at 450 °C for different times, i.e. 0, 5, 35, 335 and 1775 min, in the furnace and followed by cold water quenching. The selection of the above annealing times was following the log-normal distribution based on the JMAK empirical equations of the RX process [2]. To capture the initial grain nucleation on the specimens, a few prior tests on the other samples with the same strain were done for choosing the first observation time, i.e. 5 min annealing at 450 °C.

The samples prepared for electron backscatter diffraction (EBSD) analysis were metallographically ground by SiC papers (up to 1200 grit), then polished with ~ 40 nm OP-S (Oxide Polishing Suspensions) and finally electropolishing for 40 s in a solution of 9.5 vol% perchloric acid in ethanol at room temperature and 20 V. After each heat treatment, the annealed samples were mildly re-polished to remove the oxide layer by diluted OP-S for 30 s and electropolished for 30 s for removing ~ 10 nm in thickness. An indentation was manually put on the sample surface by diamond pen to precisely relocate the EBSD mapping at the same area.

2.2. Characterisation

Optical microscope (OM) and EBSD were applied for the microstructural characterisation. After each heat treatment, EBSD maps were captured at the same position using a Hitachi S3400N with Bruker eFlashHR EBSD Esprit v2.1 system. An accelerating voltage of 20 kV and a step size of 3 μm were applied for the EBSD mapping.

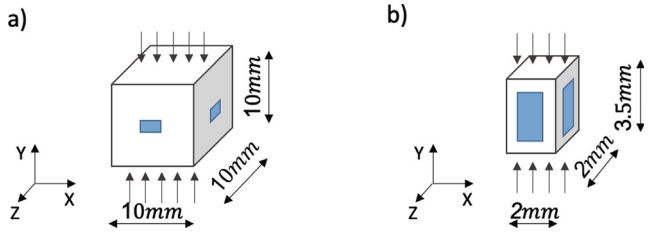

Fig. 2. a) and b) show the sample geometry of single crystal (SC) and multi-crystal (MC) samples. The positions of the corresponding EBSD maps are marked as blue boxes in the diagram. (For interpretation of the references to colour in this figure legend, the reader is referred to the web version of this article.)

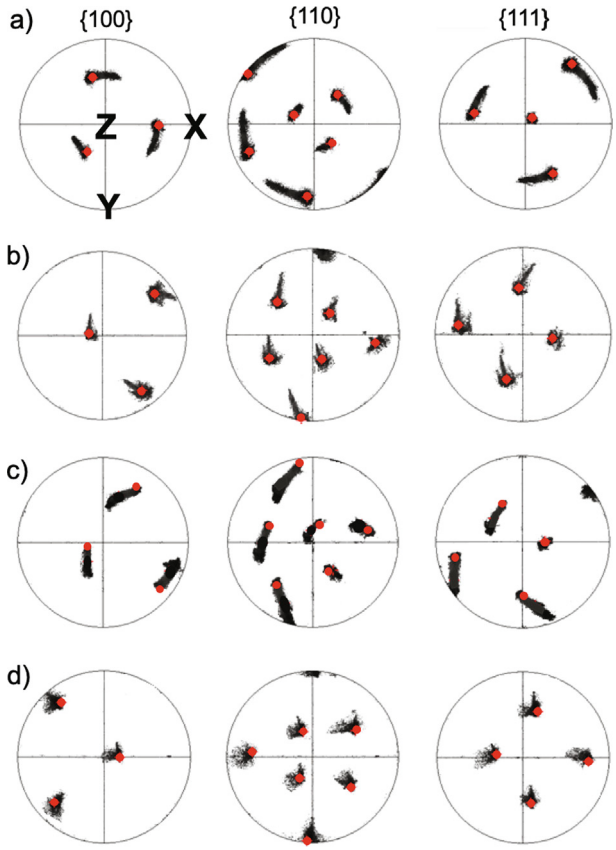

Fig. 3. a) - d) are the pole figures of SC I, II, III and IV after deformation. The red dots in pole figures show the orientation of SCs before the compression [25]. (For interpretation of the references to colour in this figure legend, the reader is referred to the web version of this article.)

2.3. KWC phase-field modelling

2.3.1. Grain nucleation

The assumption of site-saturated nucleation [34] validated by Lauridsen et al. [35] was applied in this work to simulate the grain nucleation. It means that all nucleation events of RX effectively occur at the start of recrystallization.

To find the possible nucleation sites, the stored energy distribution was calculated by Equation (6) based on the map of geometrically necessary dislocations (GNDs) obtained from the EBSD technique. The GND distribution was estimated using the method of the total line energy minimization described by Pantleon [36]. The lower bound of the GND density was estimated from the lattice rotation gradients calculated by the misorientation between the probed and its neighbouring points [36,37].

Since the high stored energy is the essential condition for the occurrence of RX [2], a critical stored energy E_c of 0.07 MPa μm^{-1} was chosen for the occurrence of grain nucleation. Also, a Gaussian distribution of misorientations of 40°–60° between the nuclei and original grains were assigned for the nuclei in this nucleation model based on the EBSD results (see Appendix Fig. A1) and literature [38]. In addition, the grain diameter of the initial nuclei was set as 30 μm which was ~ 2% to the parent grain diameter, and the minimum distance between two neighbouring nuclei was set to be 60 μm. The size of the initial nuclei was chosen based on the relative scale to the map size for the feasible computation. This relative

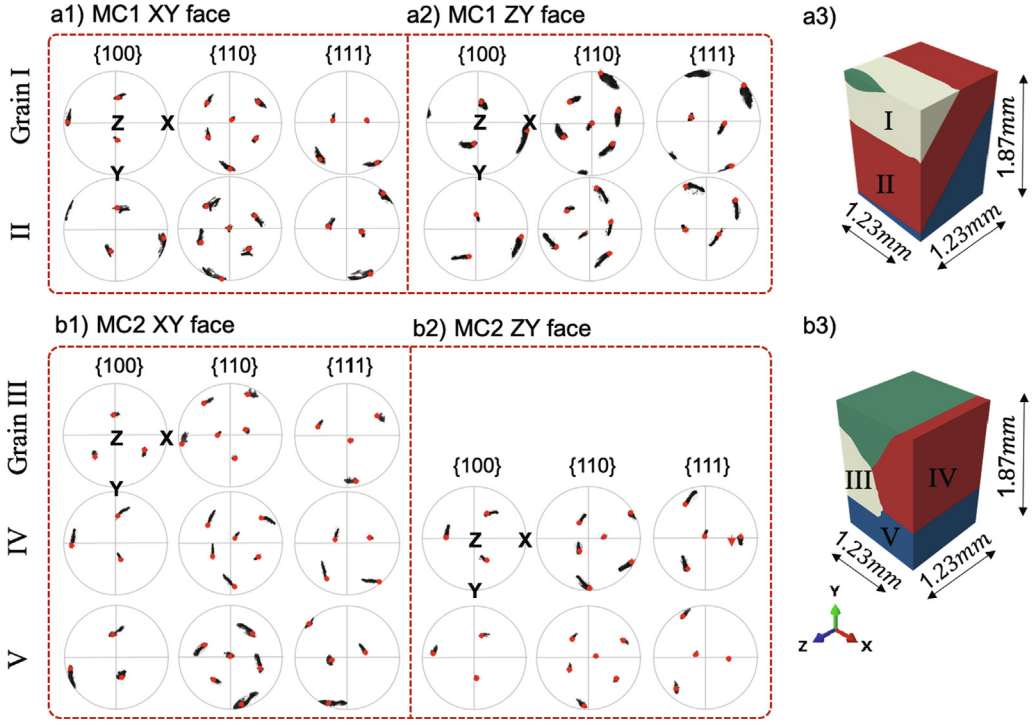

Fig. 4. a1)-a2) and b1)-b2) are PF of grains on XY and YZ face of deformed MC. Red dots in PF show the orientation before compression. a3) and b3) show the grain morphology of MC1 and MC2 in 3D [25]. (For interpretation of the references to colour in this figure legend, the reader is referred to the web version of this article.)

big size allowed the phase-field model to capture the curvature of grains at an acceptable computational cost [39].

In this work, the nucleation sites were not limited to the grain boundaries which is significantly different from the previous work [14,19]. Instead, the dislocation density is considered as the main cause of grain nucleation which introduces the lattice rotation and the stored energy.

2.3.2. Grain growth

The KWC phase-field model [21] was applied to simulate the grain growth of RX. The grain growth of nucleated grains driven by the stored energy as Equation (1) follows the time-evolution of η and θ as Equation (2) and (3) [18,40]. The variable, η, was set to be 0 for deformed grains and 1 for RXed grains. The variable, θ, was the value of $\phi_2$extracted from the Euler angle $[\phi_1, \Phi, \phi_2]$ since the model was only performed in two dimensions [21].

The free energy that contains the variablesη and θ is expressed by,

$$F = \int \left[\frac{\alpha^2}{2}|\nabla\eta|^2 + f_d(\eta) + f_e(\eta,\rho) + g(\eta)s|\nabla\theta|\right]dV \tag{1}$$

Hence, the time evolution of η and θ is given by,

$$\dot{\eta} = M_\eta\left\{\alpha^2\nabla^2\eta - \frac{\partial f_d(\eta)}{\partial\eta} - \frac{\partial f_e(\eta,\rho)}{\partial\eta} - \frac{\partial g(\eta,\rho)}{\partial\eta}s|\nabla\theta|\right\} \tag{2}$$

$$\dot{\theta} = M_\theta\frac{1}{\eta^2}\nabla\left[g(\eta)s\frac{\nabla\theta}{|\nabla\theta|}\right] \tag{3}$$

$f_e(\eta,\rho)$ in Equation (2) is the homogeneous bulk free energy term [39] expressed as,

$$f_e(\eta,\rho) = f_e^r(\rho)p(\eta) + f_e^m(\rho)(1-p(\eta)) \tag{4}$$

where $f_e(\eta,\rho)$ is an interpolation function that combines the free energy of the deformed phase $f_e^m(\rho)$ and RXed phase $f_e^r(\rho)$. $p(\eta)$ is a weight function used to smooth the density inside the interface region as,

$$p(\eta) = \eta^3(10 - 15\eta + 6\eta^2) \tag{5}$$

The free energies in deformed phase and RXed phase, $f_e^m(\rho)$ and $f_e^r(\rho)$, were calculated according to its dislocation density. The free energy in the recrystallized phase is set to be zero, i.e. $f_e^r(\rho) = 0$, since the dislocation density in the RXed grain is around five orders smaller than that of the deformed grain [20]. The free energy in the deformed phase, $f_e^m(\rho) = 50E_{store}$, has been chosen where the stored energy, E_{store}, per unit length (i.e. per micrometre) of a deformed alloy is given by Reed-Hill et al. [41],

$$E_{store} = 0.5\rho G_{12}b \tag{6}$$

where $\rho$is the dislocation density, G_{12} is the shear modulus and b is the Burger's vector magnitude of aluminium alloys.

The interfacial energy [39], $f_d(\eta)$, in Equation (2) is expressed as,

$$f_d(\eta) = Wq(\eta) \tag{7}$$

$$q(\eta) = \eta^2(1-\eta) \tag{8}$$

$$W = \frac{6\sigma a}{\delta} \tag{9}$$

where $q(\eta)$ is a double-well potential that has minima at 0 and 1, and $W$is the depth of the energy wall. Both of $q(\eta)$ and $p(\eta)$ are used to construct the homogeneous free energy density $f_e(\eta,\rho)$ [39]. The double-well coefficient, W, is modified by adjusting the grain boundary thickness, δ, and grain boundary energy, σ.

The gradient energy term, $\frac{\alpha^2}{2}|\nabla\eta|^2$, gives rise to the diffuse interface in the phase-field model. The gradient coefficient, α, in Equation (1) is a constant associated with δ and σ expressed as,

$$\alpha = \sqrt{\frac{3\delta\sigma}{a}} \tag{10}$$

where $a = 2.20$ for an interface region with $\eta \in [0.1, 0.9]$. The grain boundary thickness is given based on the theory of diffuse interface approach [39] by,

$$\delta = 4\Delta x \tag{11}$$

where Δx is the grid size. The gradient coefficient, α, and the double-well coefficient, W, were correlated directly to physical properties, such as grain boundary thickness, δ, and grain boundary energy, σ [39].

The orientation energy term, $g(\eta)s|\nabla\theta|$, in Equation (1) is given by,

$$g(\eta) = \eta^2 \tag{12}$$

$$s = \frac{6\sigma}{\pi} \tag{13}$$

where the function $g(\eta)$ is used to eliminate the effect of misorientation inside the deformed grain. The constant s is related to the interface energy, σ.

The mobilities of η and θ are expressed as M_η and M_θ. M_η that considers steady grain growth in a one dimension problem [20] is given by,

$$M_\eta = M_0 \exp\left(-\frac{Q}{RT}\right) = M_0 \exp\left(-\frac{Q'}{k_B T}\right) \tag{14}$$

Table 1
Material properties of pure aluminium on the KWC phase-field model.

Grit size (Δx)	2 μm
Grain boundary energy (σ)	0.6 J/m^2
Activation energy (Q')	2.08×10^{-19} J
Time step (Δt)	0.01 ms
Pre-exponential factor (M_0)	3.1×10^7 m^3/(N ms)

where $M_0$is a pre-exponential factor, Q and Q' are the activation energies, R is the gas constant, T is the annealing temperature and k_B is the Boltzmann constant.

The mobilities used to define the rate of change in grain orientation are defined as,

$$M_\theta = (1 - p(\eta))M_\theta^0 \tag{15}$$

$$M_\theta^0 = M_\eta \tag{16}$$

The evolution of the 2D microstructure is solved using finite difference, with an eighth-order scheme for the spatial derivatives and the Euler Forward method for time integration. The physical parameters used in the phase-field model to simulate the RX of deformed SC and MC pure aluminium at 723 K (i.e. 450 °C) are listed in Table 1.

3. Experimental results

3.1. Grain nucleation and grain growth

The deformed columnar multi-crystals and single crystals were applied to study the RX regarding the nucleation positions, nucleated grain orientations and grain growth since the effect of underlying grain orientations on the nucleated grain orientations can be avoided. For the columnar multi-crystal samples, the columnar grains on XY face expand along the Z axes. Therefore, the right big grain on the XY face is the same with the grain on YZ face (see Fig. 5).

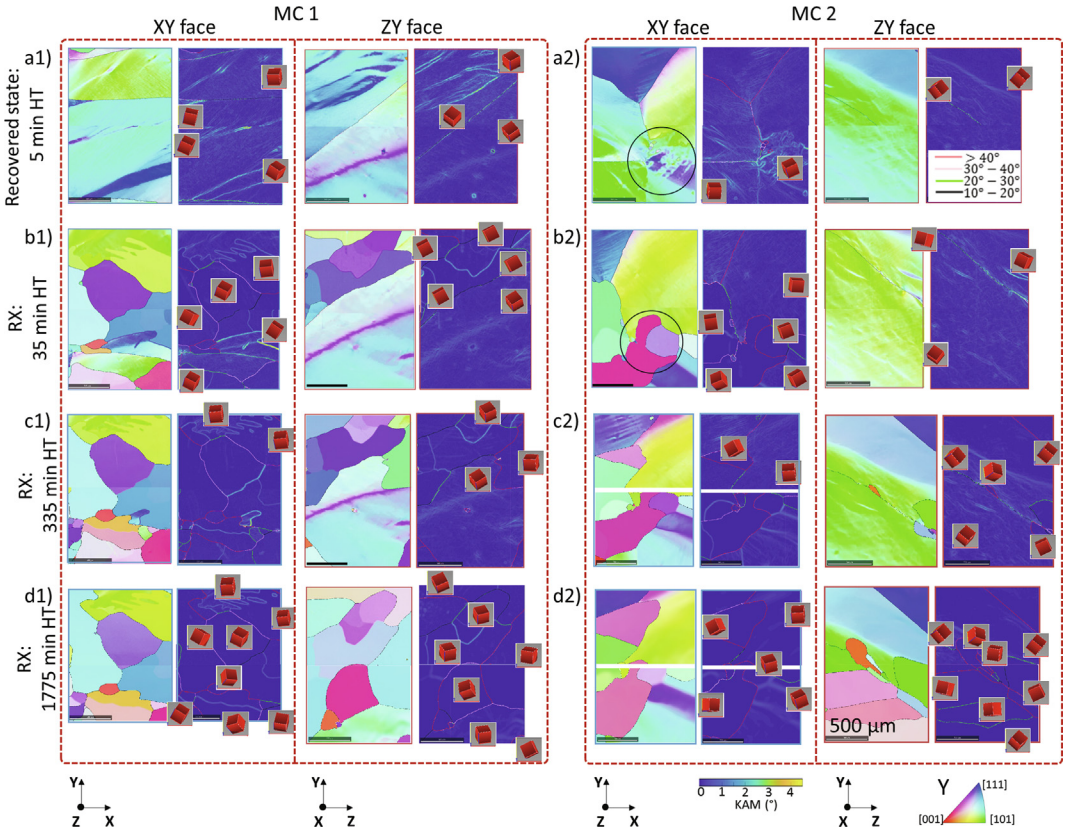

Fig. 5. a)-d) are the EBSD IPF-Y maps and their corresponding KAM maps to show the microstructure evolution on the XY and ZY faces of deformed MC1 and MC2 during the heat treatment at 450 °C for 5, 35, 335 and 1775 min. The crystal orientation information (i.e. red cubes) at each position is superimposed in the KAM maps. Also, the misorientation on grain boundaries is marked out in KAM maps. (For interpretation of the references to colour in this figure legend, the reader is referred to the web version of this article.)

To reveal the microstructural evolution of deformed MC1 and MC2 at 450 °C after different annealing times, the EBSD inverse pole figure (IPF) maps regarding its loading direction, i.e. Y-axis, and their corresponding kernel average misorientation (KAM) maps are plotted in Fig. 5. The deformed matrix mainly recovered within 5 min annealing, i.e. dislocation annihilation and arranging into dislocation walls to reduce the stored energy, thus, reducing the overall KAM values.

For the XY face of MC2 after 5 min annealing, a very beginning of grain nucleation is observed in DBs (see Fig. 5 a2)), showing lots of compact unstable nuclei on its KAM map. The initial nuclei were compact group areas formed by the recovery process that has a misorientation of ~ 5° on its boundary. The initial nuclei could accommodate dislocations and form high angle grain boundaries (i.e. > 10°) during the RX process. After 35 min annealing, stable nuclei with high misorientations on its boundaries are found in the area with DBs. For the area without DBs, such as the top half of XY and ZY faces of MC2, no grain nucleation is observed in these regions.

With further annealing to 335 min and 1775 min (see Fig. 5 c)-d)), the nucleated grains near DBs are found to grow into the deformed matrix while the initial grain boundaries are quite stable without obviously changing their shapes during annealing. The newly formed grain boundaries are noticed to have much higher mobilities compared with the initial grain boundaries.

The grains nucleated in the area with DBs can grow into 3D, for instance, the grains nucleated on the XY face of MC2 are found to grow into the ZY face (see Fig. 5 c2) and d2)). Therefore, to study the nucleated grain positions and the relation between nucleated orientation with the matrix, it is important to do the observations at the early stage of grain nucleation rather than the stage of grain growth, such as 5–35 min annealing in this work, as the observed RX grains could nucleate at somewhere else.

The EBSD IPF-Y maps for SC I-IV before and after annealing are shown in Fig. 6 where Y-axis is the uniaxial deformation direction. It has been seen that four SCs all completed the RX process within the 5 min heat treatment, while less pure MCs only finished recovery under same conditions (see Fig. 5 a1) and a2)). The SCs completed the RX process rapidly due to the absence of solutes which would retard the rate of RX.

3.2. Rxed texture

To study the texture evolution due to RX, the IPFs on the XY and ZY face of the deformed MC1 and MC2 are analysed at each stage of heat treatments (see Fig. 7), in which: the orientations from initial grains are labelled out as black arrows; the RXed orientations from DBs are labelled as red arrows; the distinctive RXed orientations which have no relation with the deformed matrix or DBs are labelled as grey dashed arrows with grey circles. Since many RXed orientations are found to be quite close to the DBs (see Fig. 5 and Fig. 7), the orientation in DBs is a major source of orientations for RXed grains in MCs.

Through comparing the IPFs of deformed and RXed SCs in Fig. 6, it is rational to conclude that the RXed orientations are partly originated from the orientations in DBs. The transitional distribution of orientation in DBs is likely to split into a few distinct orientations with misorientation ~ 10° during annealing, as shown in the evolution of IPFs on the XY face of MCs (see Fig. 7 a1) and a2)). Apart from the orientations originated from DBs, some distinctive RXed

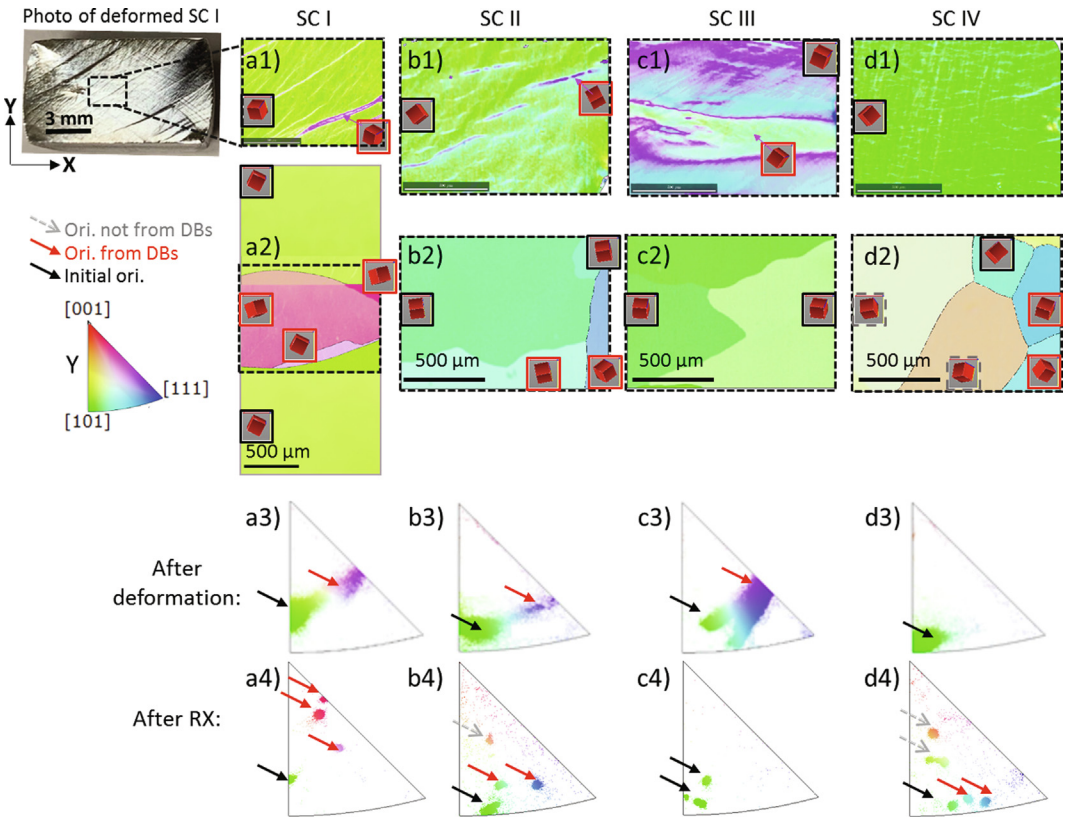

Fig. 6. a1)-d1) and a3)-d3) are the IPF maps and IPFs-Y for the deformed SC I-IV. Images reproduced with permission from Luan et al. [25], Elsevier. a2)-d2) and a4)-d4) are the IPF maps and IPFs-Y for the SC I-IV heat-treated for 5 min at 450 °C. In the IPFs, the initial orientations are marked out by black arrow, RXed orientations from DBs are marked out by red arrow and RXed orientations not from DBs are marked out by grey dashed arrow. The crystal orientation information (i.e. red cubes) at each position is superimposed in the IPF maps. The border colour of the red cubes keeps consistent with the colour legend for arrows. (For interpretation of the references to colour in this figure legend, the reader is referred to the web version of this article.)

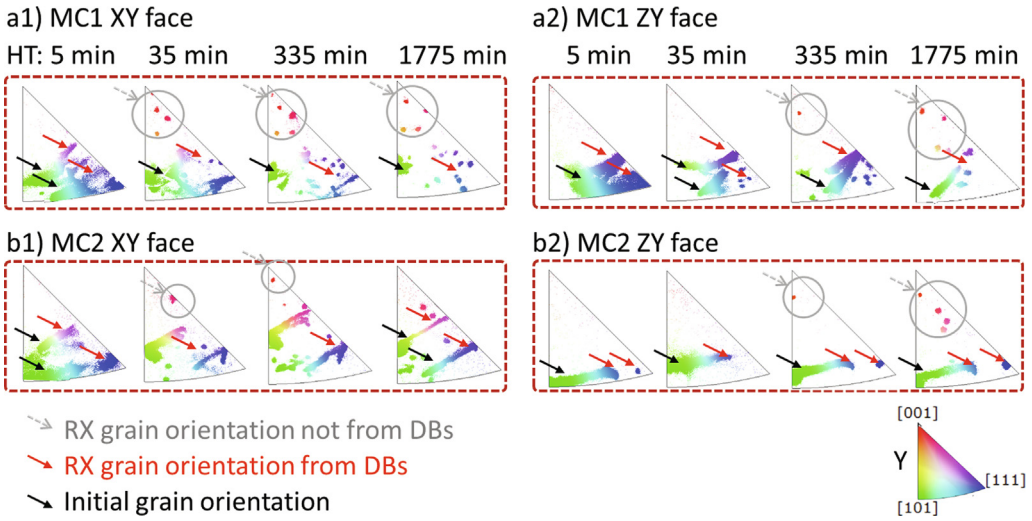

Fig. 7. a1) and a2), b1) and b2) show the evolution of IPF-Y on the XY and ZY face of the MC1 and MC2 annealing for 5, 35, 335 and 1775 min at 450 °C.

orientations are also observed in MCs which are clearly neither from the initial grain orientation nor the DBs.

3.3. Distinctive RX grain orientations

In an association of Fig. 5 and Fig. 7, it can be seen that the distinctive RXed orientations in Fig. 7 are mainly located at the bottom free surface of the specimen as shown in Fig. 5 which is the contacting area during compression.

To make sure that those distinctive orientations were generated at the bottom free surface of the specimen, extra EBSD maps for MC1 and MC2 were taken at the bottom free surface area of the ZY faces after 35 and 1775 min annealing (shown in Fig. 8). The contacting area with the compression stage is marked out by an array of black slashes in Fig. 8. It has been seen that nearly all the distinctive RXed orientations are found in this bottom free surface area. For example, in MC2 (see IPF-Y in Fig. 8 b), the distinctive orientations are labelled by red colour. In comparison, all the RXed

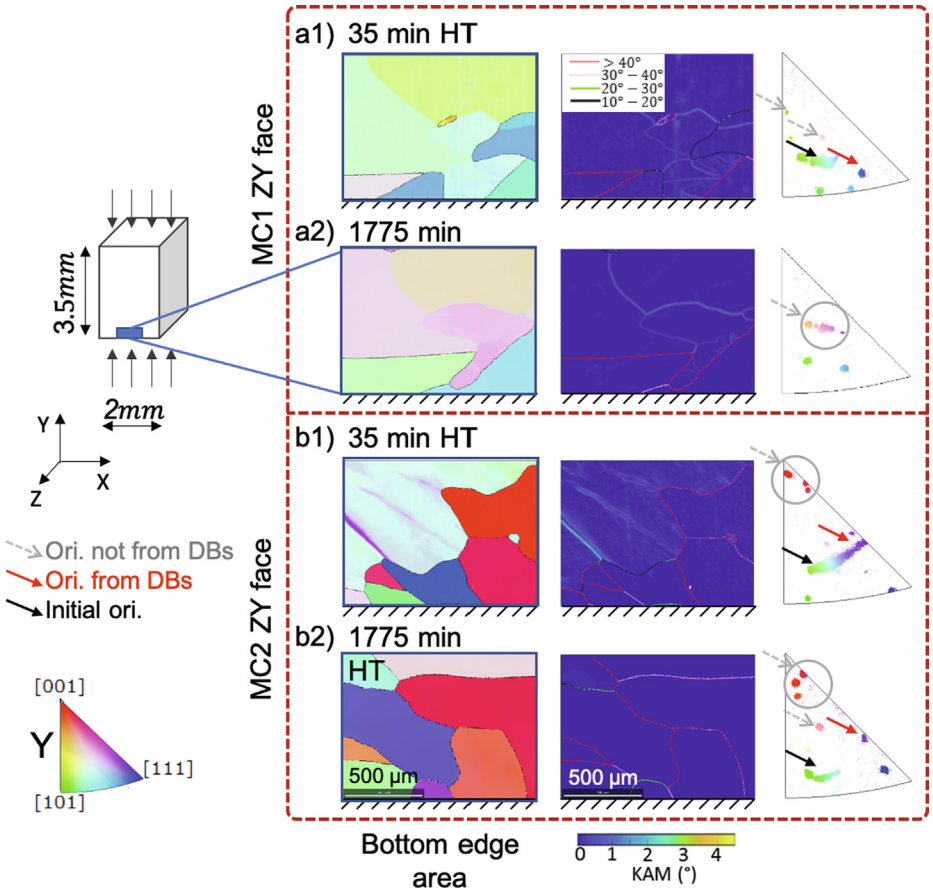

Fig. 8. a1)-a2) and b1)-b2) show the IPF-Y maps, KAM maps and IPFs-Y of the bottom free surface area on the ZY face of MC1 and MC2, respectively. Colours mark out the misorientations on the grain boundaries in KAM maps.

grains with red colour in MC2 are located near the contacting area of compression.

Furthermore, as shown in the KAM maps in Fig. 8, the grain boundaries of distinctive RXed grains are found to have high misorientation > 40°. Through comparing a1)-a2) and b1)-b2) in Fig. 8, these grains at the bottom free surface area are found to grow quickly into the inside of the specimen during annealing.

4. Quantitative analysis

The whole XY and ZY face of the MC1 and MC2 are separated into two areas, i.e. top and bottom area, to quantitatively analyse the effect of DBs on the grain nucleation and grain growth (see Fig. 9 and Fig. 10). The abscissa in those figures represents the annealing time (seconds) in the logarithmic form showing as log(s).

4.1. Observed grain nucleation

The microstructure of each area after 0, 5, 35, 335 and 1775 min annealing at 450 °C are analysed respectively for the evolution of grain size, high angle grain boundary (HAGB) fraction and the number of grains. The eight EBSD maps for the top and bottom area are divided into two groups: one group is the area with DBs (see the left column plots in Fig. 9 and Fig. 10, including the bottom area of the XY face in MC2, the top area of the ZY face in MC1, the bottom and the top area of the XY face in MC1); the other group is the area without the existence of DBs (see the right column plots in Fig. 9 and Fig. 10, including the bottom area of the ZY face in MC1, the whole ZY face and the top area of the XY face in MC2).

The sudden change of the grain diameter, HAGB fraction and the number of grains indicates the occurrence of RX [42]. By comparing the left and right columns in Fig. 9 and Fig. 10 a1), it can be seen that notable RX was found at 35 min annealing in the areas with DBs while no obvious RX was found in the areas without DBs. By contrast, the change of grain size and HAGB fraction was found at 335 min in those areas (see Figure 9 a2) and Figure 10 a2)), showing that the RXed grains were found much later in the areas without DBs than the areas with DBs. These observations are also verified by the grain structure maps shown in Fig. 5.

It also has been found in Figure 9 a1)-a2) and Fig. 10 a1)-a2) that the RX process would result in the decrease of average grain diameter (i.e. the increase of the number of grains and the increase of HAGB fraction) in pure aluminium. The slight increase of grain diameter and drop of HAGB fraction from 335 min to 1775 min annealing are attributed to the grain growth of nucleated grains in the early stage of annealing.

4.2. Simulated grain nucleation

The grain nucleation was simulated based on the nucleation laws discussed in Section 2.3.1 to generate the heterogeneous distribution of nucleated grains as shown in Appendix Fig. A1. In Fig. 11, the number of simulated nucleated grains are compared with the misorientation angle, and the area fraction of DBs measured from EBSD maps for each face of MC. The nucleated grain number is found to be more closely correlated with the area fraction of DBs in comparison to the misorientation angle.

4.3. Simulated grain evolution

The simulated microstructural evolutions are plotted in Fig. 10 b1)-b2) for the areas with and without the existence of DB. The

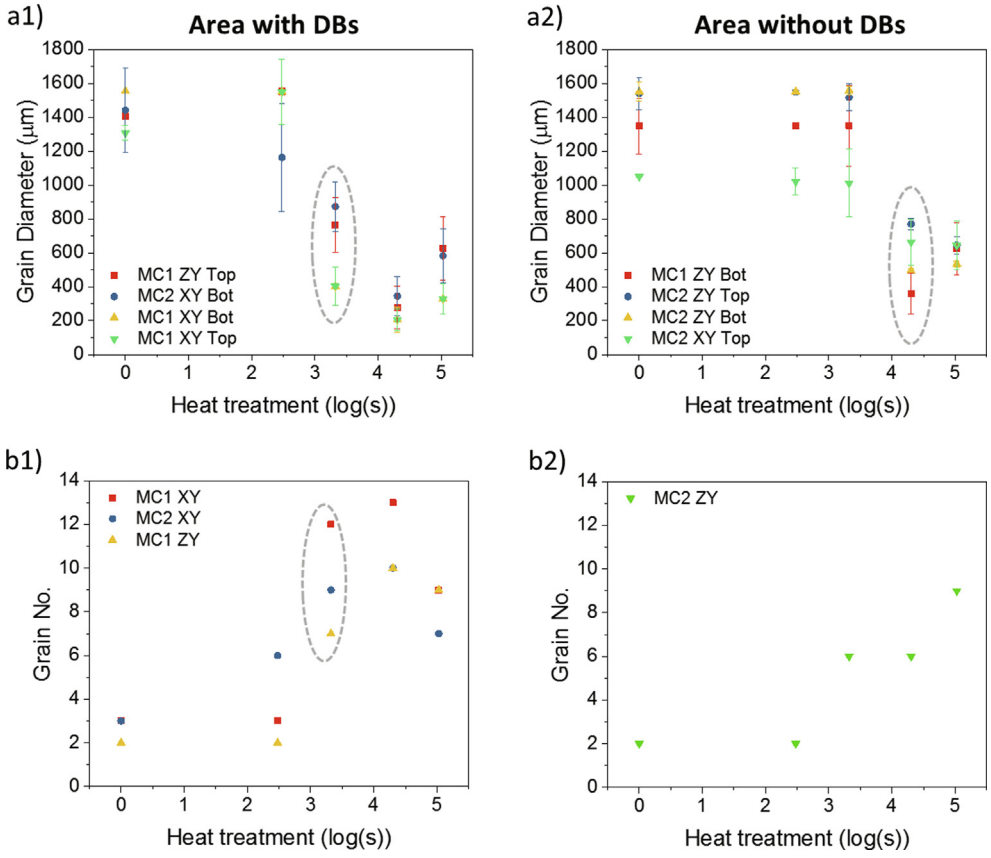

Fig. 9. a1)-b1) show the evolution of grain diameter in the areas with and without distinct DBs; b1) and b2) show the evolution of the total number of grains on the faces with DBs and the face without DBs. The values with obvious changes during annealing are circled out in plots. The area fraction of DBs in MC2 ZY Top, MC2 XY Bot, MC1 XY Top and MC1 XY Top is from high to low.

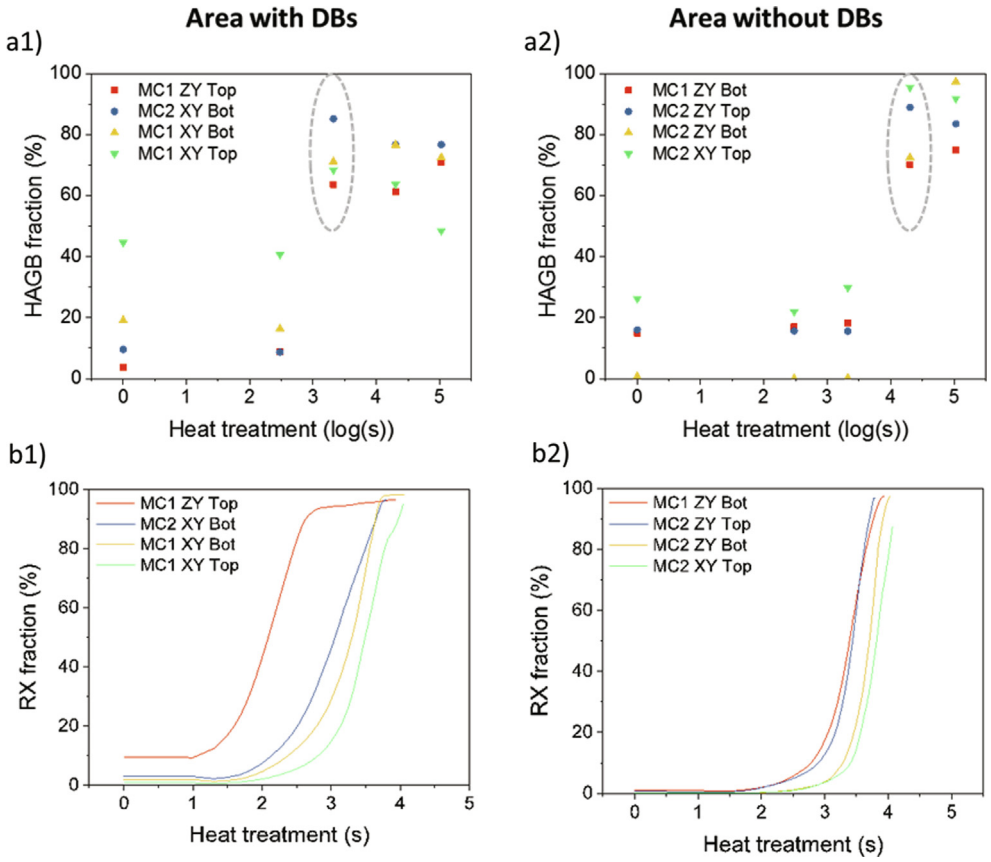

Fig. 10. a1)-a2) show the evolution of the HAGB fraction in the area with DBs and without DBs in experimental results; b1) and b2) show the simulated evolution of the RX fraction in the area with DBs and without DBs. The area fraction of DBs in MC2 ZY Top, MC2 XY Bot, MC1 XY Top and MC1 XY Top is from high to low.

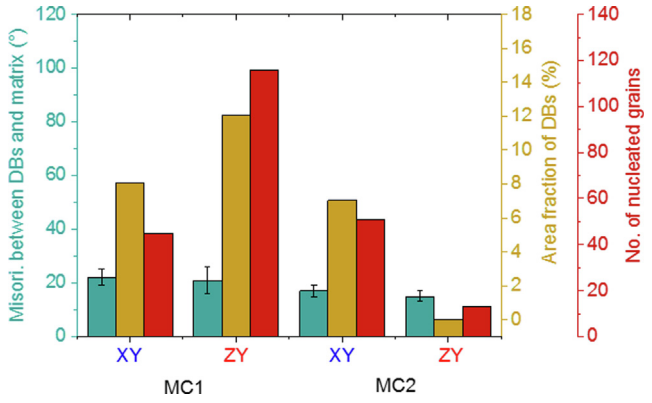

Fig. 11. Comparison of misorientation angle on the boundary of DBs and area fraction of DBs with the simulated nucleated grain no. on XY and ZY face of MC1 and MC2.

coloured lines in the legend from top to bottom represent the descending order of the area fraction of DBs (i.e. from high to low). It can be seen from the simulations that the areas with a higher volume fraction of DBs show an earlier start and quicker finish of RX, i.e. lines from left to right for the colour red, blue, yellow and green respectively in Fig. 10.

The simulated RX process by this KWC phase-field model has a good agreement with the experimental observations by quasi-in-situ EBSD maps. For the areas with distinct DBs in MCs, it has been found that the RX mainly occurs around 1000 s (i.e. 16.7 min) and completes before 10000 s (i.e. 166.7 min) in both of experimental results (see Fig. 10 a1) and in simulation results (see Fig. 10 b1). However, for areas without distinct DBs, nearly none obvious RX is found around 1000 s (i.e. 16.7 min) in both of experimental results (see Fig. 10 b1) and simulation results (see Fig. 10 b2).

5. Discussions

5.1. Rxed orientations

According to the IPF evolution of the RX process in MCs (see Fig. 7) and SCs (see Fig. 6), it has been found that the majority of RXed orientations, which are a group of orientations with misorientation ~ 10° between each other, are originated from the orientation in DBs. Hence, orientation in DBs provides a source of orientations for RXed grains. In our previous work [25], it has been demonstrated that the orientations in DBs are rotated from the initial orientation whose {1 1 1} slip planes are likely to become perpendicular to the loading direction.

To study the source of RXed orientations, it is important to capture all deformed orientations for the analysation since the RXed grains nucleated at DBs would grow into the deformed matrix in 3D and can be found somewhere else. For example, the grains nucleated on the XY face of MC2 after 335 min annealing is found to grow into the ZY face along the initial grain boundary (see Figure 5 c2) and d2)).

Besides of the RXed orientations from DBs, some distinctive RXed orientations, which are apparently with no relation to the orientations of DBs and deformed matrix, are observed in the RXed microstructure (see Fig. 5 and Fig. 7). After checking the RXed

microstructure near the compressive free surface of samples, it has been found that nearly all these distinctive orientations are located near the contacting area with the compression stage in Fig. 8.

The distinctive RXed orientations are formed likely due to the compressive friction at the contacting area of the specimen with the compression stage. The unavoidable localised friction could distort the lattice structure and create new orientations at the contacting layer during the compression [42]. Those new orientations in our work are found to have high misorientations $\sim 40^{\circ}$ at the grain boundaries (i.e. HAGBs) and could grow fast into the matrix during annealing (see Fig. 8) since the HAGBs have been demonstrated to have much higher mobility compared with LAGBs (i.e. low angle grain boundaries) [43,44]. Additionally, the free surface of the specimen apparently has a higher heating rate compared with the inside of the specimen when the heating is conducted in the furnace. The grains near the free surface, therefore, would have a higher driving force for the grain growth compared with the inside grains at the beginning of heating.

In summary, the RXed grain orientations are generated from two sources: one is from the DBs; the other one is from the contacting free surface of the specimen due to compressive frictions.

5.2. Grain nucleation

The quasi-in-situ EBSD maps of deformed MC1 and MC2 in Fig. 5 clearly show the positions of grain nucleation in deformed pure aluminium. It has been seen that the nucleated grains are more likely to germinate in the DBs after 35 min annealing at 450 °C, rather than at the initial grain boundaries. Thus, it has been demonstrated in this work that initial grain boundaries, compared with DBs, are not favourable nucleation sites for pure aluminium. This finding is against many discussions in previous studies from which only grain boundaries are considered for the grain nucleation [4,5].

Instead, the initial grain boundaries act quite stable during heat treatment without incubating new grains and having obvious movements. This stable characteristic could also demonstrate that the initial grain boundaries are not potential sites for the grain nucleation at the early RX. Even though the misorientation angles on initial grain boundaries are high, the neatly arranged dislocations on the initial boundaries would make newly formed dislocations during deformation hard to move across them. Therefore, in comparison to DBs, the initial grain boundaries are not potential sites for nucleation. By contrast, they act as barriers for the nucleated grains to grow across. For those few RXed grains observed near the grain boundaries after longstanding annealings, such as the small grains found in the ZY face of MC2 after 335 min annealing shown in Figure 5 c2), they could be attributed to the growth of RXed grains which nucleated in DBs since their orientations are quite close the orientation of DBs.

The RXed grains once nucleated in DBs would grow into the deformed matrix and reduce the stored energy of the system during further annealing. That is why the RXed grains with the orientations close to DBs are also found in the area without DBs but with much longer annealing (as shown in the plots of Fig. 9). Therefore, it is rational to conclude that the grain nucleation in the deformed pure aluminium prefers to occur at the DBs, which contains both high orientation gradients and heterogeneous strain distribution.

According to this finding, assumptions for the simulation of grain nucleation made in many previous computational models [8,20] need to be revised, which only considered the grain boundaries as the potential nucleation sites for the RX simulation. The dislocation structure, particularly the DBs, should be taken into account for the simulation of grain nucleation.

The effect of DBs on grain nucleation has been studied in Fig. 11. The number of nucleated grains is found to have a correlation with the area fraction of DBs while no obvious correlation is observed for the misorientation angle between DBs and deformed matrix.

5.3. Grain growth

As shown in experimental results (see Fig. 5 and Fig. 9), the grains nucleated in DBs are found to grow into the deformed matrix and sometimes grow along the initial grain boundary during further annealing.

In this KWC phase-field modelling work, the EBSD maps of the deformed samples are directly imported into the model [45] as the deformed microstructure for the occurrence of RX. Moreover, this KWC phase-field model combines sound physical concepts for the prediction of RX kinetics which is unlike the empirical approaches and probabilistic based models such as Monte Carlo Potts model [16,17,46] and cellular automata model [47,48]. In this model, the concept of energy minimisation is written as a physically-based thermodynamic equation for the prediction of microstructural evolution during annealing. It includes the energy from dislocations, misorientations, grain boundaries and gradient field of phases. The arbitrary grain boundary geometries and their evolution with physical time step and length scale are simulated well by this model for the whole RX process.

The kinetics of grain growth is checked for all the areas with and without distinct DBs by experimental EBSD analysis (see Fig. 9 and Fig. 10 a)) and KWC phase-field modelling (see Fig. 10 b)). It has been validated by the series of EBSD maps that this KWC phase-field model has successfully simulated the whole RX process for all areas on MC1 and MC2 regarding the annealing time.

The kinetics of grain growth has also been found to have a strong correlation with the area fraction of DBs. As shown in Fig. 10 b1)-b2), the areas with DBs are found to complete the RX process much earlier than the areas without distinct DBs, i.e. the higher the area fraction of DBs is, the quicker the RX process could finish. Since the grain nucleation prefers to occur in the DBs, more nucleated grains would be found in the area with DBs resulting in a faster evolution of the RX fraction. This positive correlation between the number of nucleated grains and the area fraction of DBs has been demonstrated in discussions about grain nucleation (see Section 5.2).

5.4. RX mechanism

Through capturing the microstructural changes of the whole deformed area by quasi-in-situ EBSD maps for SCs and MCs, it has been observed that the grain nucleation is likely to initially occur inside the DBs and grow into the deformed matrix. Such that, RX in the area with DBs is found to be much quicker than the area without DBs.

The mechanism of RX in grain level is summarised in Fig. 12 to explain the above observations of RX process at the existence of DBs for pure aluminium. The sequence of a)-d) in Fig. 12 shows the four steps which are relative to the RX process: a) the formation of DBs in plastically deformed crystal as a result of the intersection of two types of activated slip systems (i.e. red and black symbol), as well as the dislocation pile-up at the intersection area [25]; b) the formation of unstable subgrains inside the DBs due to the substantial dislocations blocked in the DBs. This step is recognised as the initial recovery during annealing.

Fig. 12 c) shows the formation of HAGBs due to the growth of subgrains, as well as the formation of subgrains at the outer layer of DB. The formation of subgrains at the outer layer of DB is slower than the inner layer of DBs since the outer layer contains less blocked dislocations, thus, requires more incubation time for the formation of subgrains [2,49]. In order to eliminate the excess dis-

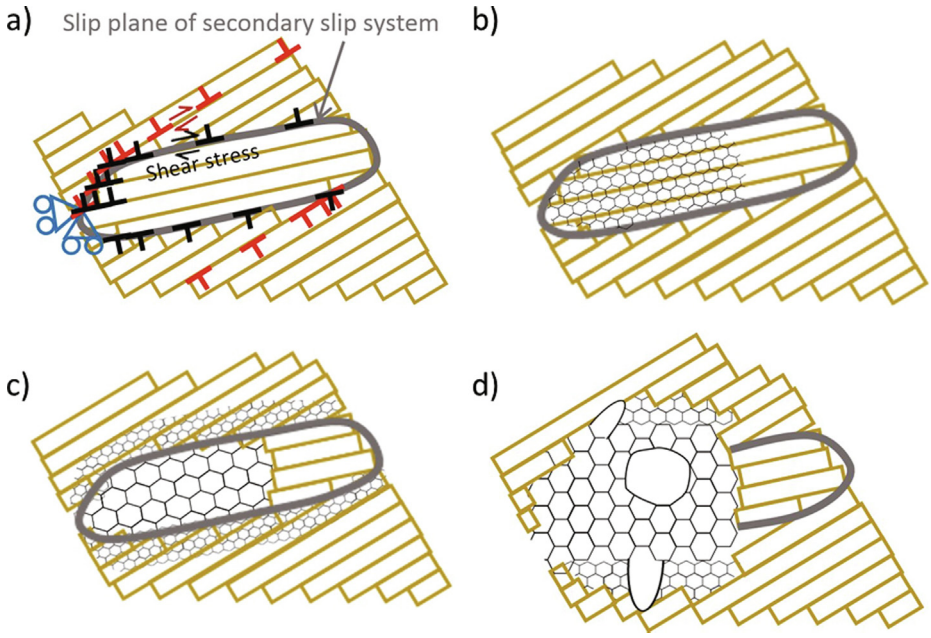

Fig. 12. Schematics to show the relative steps to the RX process: a) the formation of DB due to slip band intersection and dislocation pile-up at the intersection area. Image reproduced with permission from [25], Elsevier; b) initial recovery for the formation of unstable subgrains in the DB; c) RX for the formation of HAGBs and later recovery at the outer layer of DB; d) RX and grain growth during annealing.

locations at subgrain walls, the larger RXed grains formed in DBs are likely to consume the later formed subgrains at the outer layer of DBs following the mechanism of strain-induced boundary migration (SIBM) discussed in [4]. The orientations of RXed grains in Fig. 7 which are found to be close to the orientations in DBs can be treated as a proof for this phenomena.

Fig. 12 d) shows the combination of RX, grain growth by the SIBM [50] and subgrain boundary migration [51,52]. It contributes to the primary and secondary grain growth for the development of final microstructure [2].

6. Conclusions

In this work, the quasi-in-situ EBSD maps of the whole deformed sample surface are applied to study how the DBs affect the recrystallization in deformed pure aluminium. It has been found that:

1. The orientation of DBs is demonstrated to be a major source of orientations for the RXed grains which would eventually contribute to the RXed texture.
2. The grain nucleation prefers to occur in DBs in the comparison with the initial grain boundaries since the developed DBs contains more unstable dislocations than the initial grain boundary.
3. Demonstrated by both of experiments and modelling, the areas with higher area fraction of DBs are found to complete the RX process much quicker than the area without DBs since DBs would provide more potential nucleated sites and less incubation time for RX.
4. It has been found that the number of nucleated grains has a strong positive correlation with the area fraction of DBs while no obvious correlation is found for the misorientation angle in KWC phase-field modelling.

Data availability

The raw/processed data required to reproduce these findings cannot be shared at this time due to technical or time limitations.

CRediT authorship contribution statement

Qinmeng Luan: Conceptualization, Data curation, Formal analysis, Investigation, Methodology, Project administration, Validation, Visualization, Writing - original draft, Writing - review & editing. **Jianglong Wang:** Writing - review & editing. **Yan Huang:** Methodology, Writing - review & editing. **Daniel S. Balint:** Writing - review & editing. **Jun Jiang:** Conceptualization, Project administration, Supervision, Writing - review & editing.

Declaration of Competing Interest

The authors declare that they have no known competing financial interests or personal relationships that could have appeared to influence the work reported in this paper.

Acknowledgements

The strong support from the Aviation Industry Corporation of China (AVIC), the First Aircraft Institute (FAI), China Scholarship Council (CSC), the Henry Lester Trust and the Great Britain-China Educational Trust for this funded research is much appreciated. The research was performed at the AVIC Centre for Structural Design and Manufacture at Imperial College London. Qinmeng Luan would gratefully thank Junyi Lee for his assistance on KWC phase-field modelling and like to thank Dr Ruth Brooker for training and support of the instrument. Qinmeng Luan also thanks Yuanyuan Li for the advice on the layout of figures. Jun Jiang would like to thank EPSRC for the funding from the LightForm program: EP/R001715/1.

Appendix

Fig. A1 and Fig. B1

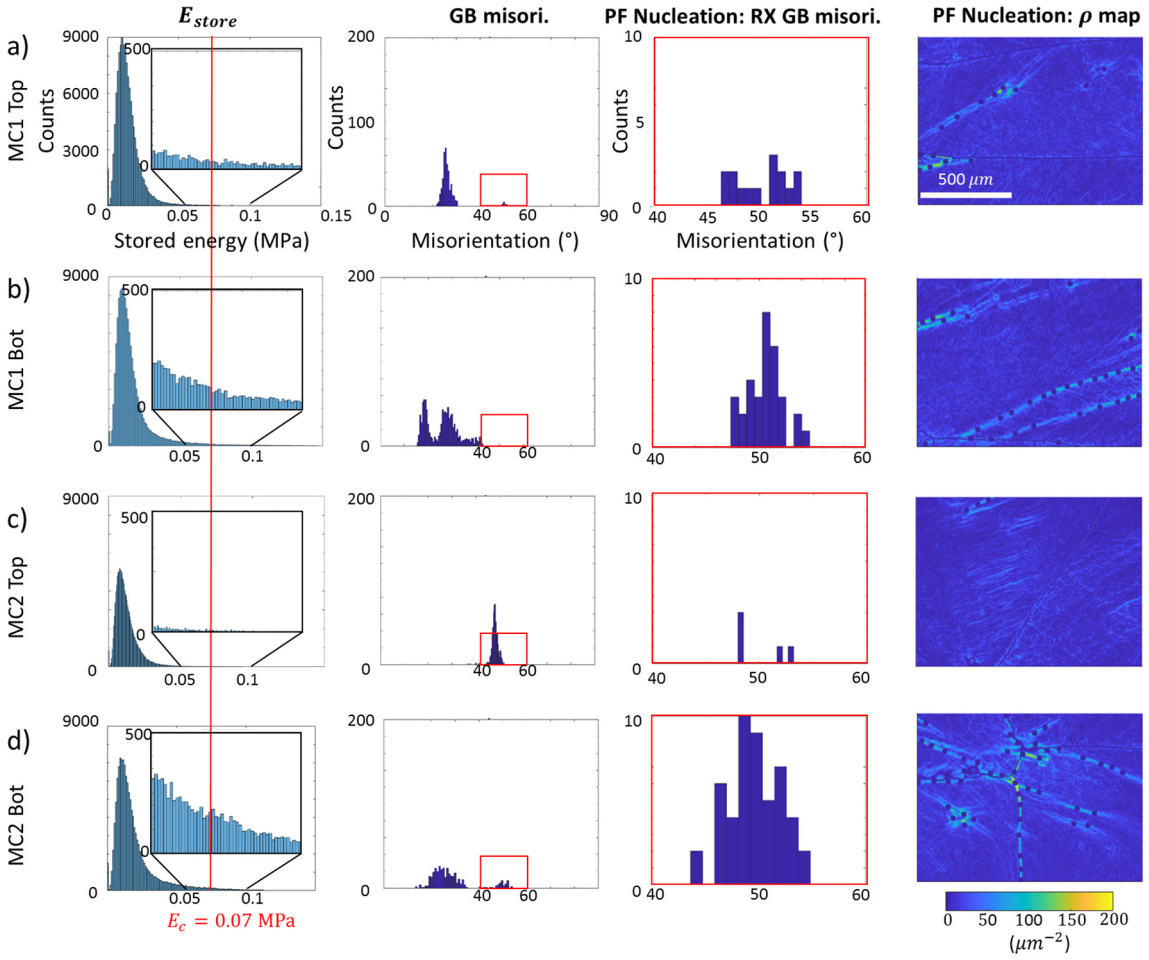

Fig. A1. Schematics to show how grain nucleation conditions applied for the XY faces of deformed MC1 and MC2. The 1st-row shows the stored energy distribution of deformed specimens; 2nd-row shows the misorientation distributions calculated based on EBSD maps; 3rd-row shows the misorientation distribution of the simulated nucleated grains following the Gaussian distribution law; 4th-row is the GND distributions after seeding to show the seeding positions.

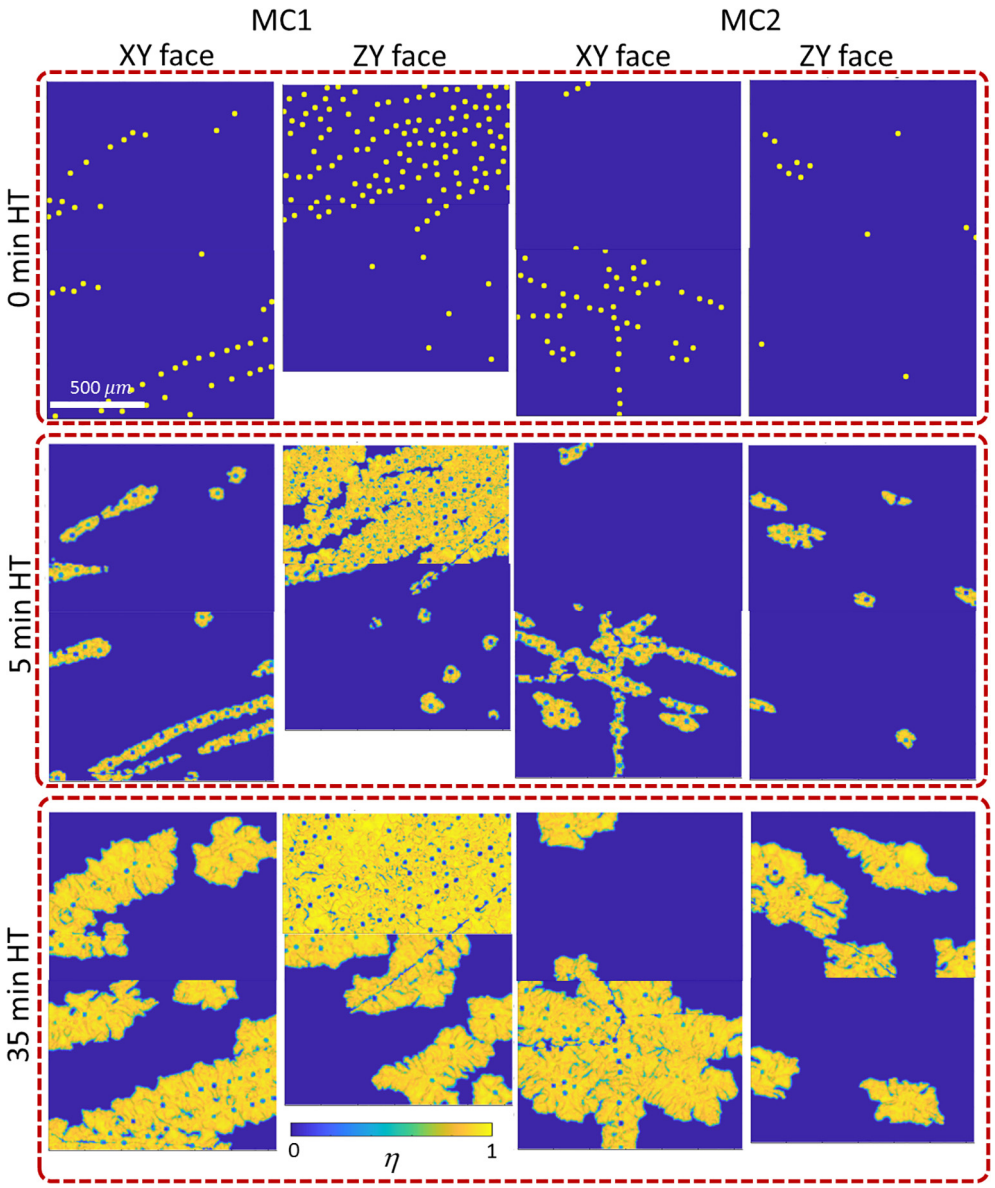

Fig. B1. KWC phase-field simulated evolution of RXed phase during annealing in XY and side face of MC1 and MC2.

References

[1] H.J. Scheel, The Development of Crystal Growth Technology, in: Cryst. Growth Technol., John Wiley & Sons, Ltd, Chichester, UK, 2003: pp. 1–14. 10.1002/0470871687.ch1.

[2] F.J. Humphreys, M. Hatherly, Recrystallization and related annealing phenomena, Elsevier (2004), https://doi.org/10.1016/B978-008044164-1/50014-1.

[3] H. Hallberg, Approaches to modeling of recrystallization, Metals (Basel). 1 (2011) 16–48, https://doi.org/10.3390/met1010016.

[4] P.R. Rios, F. Siciliano, H. Ricardo, Z. Sandim, R.L. Plaut, A. Fernando Padilha, Nucleation and growth during recrystallization, Mater. Res. 8 (2005) 225–238. 10.1590/S1516-14392005000300002.

[5] B. Bay, N. Hansen, Recrystallization in Commercially Pure Aluminum, Metall. Trans. A 15 (1984) 287–297, https://doi.org/10.1007/BF02645114.

[6] M. Miszczyk, H. Paul, J.H. Driver, C. Maurice, New orientation formation and growth during primary recrystallization in stable single crystals of three face-centred cubic metals, Acta Mater. 83 (2015) 120–136, https://doi.org/10.1016/j.actamat.2014.09.054.

[7] M.M.M. Miszczyk, H. Paul, J.H.H. Driver, P. Drzyma, P. Drzymała, Recrystallization nucleation in stable aluminium-base single crystals : Crystallography and mechanisms, Acta Mater. 125 (2017) 109–124, https://doi.org/10.1016/j.actamat.2016.11.054.

[8] K. Kashihara, M. Tagami, T. Okada, F. Inoko, Nucleation of recrystallized grains in multiple slipped structure without deformation band in aluminum single crystal, Mater. Sci. Eng., A 291 (2000) 207–217, https://doi.org/10.1016/S0921-5093(00)00961-8.

[9] C.D. Barrett, A. Imandoust, A.L. Oppedal, K. Inal, M.A. Tschopp, H. El Kadiri, Effect of grain boundaries on texture formation during dynamic recrystallization of magnesium alloys, Acta Mater. 128 (2017) 270–283, https://doi.org/10.1016/J.ACTAMAT.2017.01.063.

[10] D. Guan, W.M. Rainforth, J. Gao, L. Ma, B. Wynne, Individual effect of recrystallisation nucleation sites on texture weakening in a magnesium alloy: Part 2- shear bands, Acta Mater. 145 (2018) 399–412, https://doi.org/10.1016/j.actamat.2017.12.019.

[11] A.D. Rollett, Overview of modeling and simulation of recrystallization, Prog. Mater Sci. 42 (1997) 79–99, https://doi.org/10.1016/S0079-6425(97)00008-X.

[12] P. Zhao, Y. Wang, S.R. Niezgoda, Microstructural and micromechanical evolution during dynamic recrystallization, Int. J. Plast. 100 (2018) 52–68, https://doi.org/10.1016/J.IJPLAS.2017.09.009.

[13] P. Zhao, T. Song En Low, Y. Wang, S.R. Niezgoda, An integrated full-field model of concurrent plastic deformation and microstructure evolution: Application to 3D simulation of dynamic recrystallization in polycrystalline copper, Int. J. Plast. 80 (2016) 38–55. 10.1016/J.IJPLAS.2015.12.010.

[14] X. Zhou, H. Zhang, G. Wang, X. Bai, Y. Fu, J. Zhao, Simulation of microstructure evolution during hybrid deposition and micro-rolling process, J. Mater. Sci. 51 (2016) 6735–6749, https://doi.org/10.1007/s10853-016-9961-0.

[15] T. Takaki, T. Hirouchi, Y. Hisakuni, A. Yamanaka, Y. Tomita, Multi-Phase-Field Model to Simulate Microstructure Evolutions during Dynamic Recrystallization, Mater. Trans. 49 (2008) 2559–2565, https://doi.org/10.2320/matertrans.MB200805.

[16] K. Adam, D. Zöllner, D.P. Field, 3D microstructural evolution of primary recrystallization and grain growth in cold rolled single-phase aluminum alloys, Model. Simul. Mater. Sci. Eng. 26 (2018), https://doi.org/10.1088/1361-651X/aaa146.
[17] D. Raabe, Multiscale recrystallization models for the prediction of crystallographic textures with respect to process simulation, J. Strain Anal. Eng. Des. 42 (2007) 253–268, https://doi.org/10.1243/03093247JSA219.
[18] Q. Luan, J. Lee, Z. Zheng, J. Lin, J. Jiang, Static recrystallization study on pure aluminium using crystal plasticity finite element and phase-field modelling, Procedia Manuf. 15 (2018) 1800–1807, https://doi.org/10.1016/j.promfg.2018.07.211.
[19] E. Popova, Y. Staraselski, A. Brahme, R.K. Mishra, K. Inal, Coupled crystal plasticity – Probabilistic cellular automata approach to model dynamic recrystallization in magnesium alloys, Int. J. Plast. 66 (2015) 85–102, https://doi.org/10.1016/J.IJPLAS.2014.04.008.
[20] T. Takaki, A. Yamanaka, Y. Higa, Y. Tomita, Phase-field model during static recrystallization based on crystal-plasticity theory, J. Comput. Mater. Des. 14 (2007) 75–84, https://doi.org/10.1007/s10820-007-9083-8.
[21] Q. Luan, J. Lee, J.-H. Zheng, C. Hopper, J. Jiang, Combining microstructural characterization with crystal plasticity and phase-field modelling for the study of static recrystallization in pure aluminium, Comput. Mater. Sci. (2019), https://doi.org/10.1016/J.COMMATSCI.2019.109419 109419.
[22] J. Friedel, Dislocations, Elsevier Science, 1964.
[23] C.S. Barrett, L.H. Levenson, Structure of iron after drawing, swaging and elongation in tension, Trans. Aime. 135 (1939) 327–352.
[24] N. Jia, P. Eisenlohr, F. Roters, D. Raabe, X. Zhao, Orientation dependence of shear banding in face-centered-cubic single crystals, Acta Mater. 60 (2012) 3415–3434, https://doi.org/10.1016/j.actamat.2012.03.005.
[25] Q. Luan, H. Xing, J. Zhang, J. Jiang, Experimental and crystal plasticity study on deformation bands in single crystal and multi-crystal pure aluminium, Acta Mater. 183 (2020) 78–92, https://doi.org/10.1016/J.ACTAMAT.2019.11.006.
[26] Y. Guo, J. Schwiedrzik, J. Michler, X. Maeder, On the nucleation and growth of 11–22 twin in commercial purity titanium: In situ investigation of the local stress field and dislocation density distribution, Acta Mater. 120 (2016) 292–301, https://doi.org/10.1016/j.actamat.2016.08.073.
[27] Y. Guo, D.M. Collins, E. Tarleton, F. Hofmann, A.J. Wilkinson, T. Ben Britton, Dislocation density distribution at slip band-grain boundary intersections, Acta Mater. 182 (2020) 172–183, https://doi.org/10.1016/J.ACTAMAT.2019.10.031.
[28] F. Di Gioacchino, J. Quinta da Fonseca, Plastic Strain Mapping with Sub-micron Resolution Using Digital Image Correlation, Exp. Mech. 53 (2013) 743–754, https://doi.org/10.1007/s11340-012-9685-2.
[29] J.B. Hess, C.S. Barrett, Structure and nature of kink bands in zinc, JOM 1 (1949) 599–606, https://doi.org/10.1007/BF03398902.
[30] K. Higashida, J. Takamura, N. Narita, J. Takamurat, N. Narita, The Formation of Deformation Bands in f. c. c, Crystals, Elsevier (1986), https://doi.org/10.1016/0025-5416(86)90266-1.
[31] K. Mecke, C. Blochwitz, Saturation Dislocation Structures in Cyclically Deformed Nickel Single Crystals of Different Orientations, Cryst. Res. Technol. 17 (1982) 743–758, https://doi.org/10.1002/crat.2170170610.
[32] K. Hagihara, M. Yamasaki, M. Honnami, H. Izuno, M. Tane, T. Nakano, Y. Kawamura, Philosophical Magazine Crystallographic nature of deformation bands shown in Zn and Mg-based long-period stacking ordered (LPSO) phase Crystallographic nature of deformation bands shown in Zn and Mg-based long-period stacking ordered (LPSO) phase, (2014). 10.1080/14786435.2014.987843.
[33] Y. Yang, L. Wang, T.R. Bieler, P. Eisenlohr, M.A. Crimp, Quantitative Atomic Force Microscopy Characterization and Crystal Plasticity Finite Element Modeling of Heterogeneous Deformation in Commercial Purity Titanium, Metall. Mater. Trans. A 42 (2011) 636–644, https://doi.org/10.1007/s11661-010-0475-0.
[34] K. Marthinsen, E. Nes, O. Daaland, T. Furu, The spatial distribution of nucleation sites and its effect on recrystallization kinetics in commercial aluminum alloys, Metall. Mater. Trans. A 34 (2003) 2705–2715, https://doi.org/10.1007/s11661-003-0172-3.
[35] E.M. Lauridsen, H.F. Poulsen, S.F. Nielsen, D. Juul Jensen, Recrystallization kinetics of individual bulk grains in 90% cold-rolled aluminium, Acta Mater. 51 (2003) 4423–4435, https://doi.org/10.1016/S1359-6454(03)00278-7.
[36] W. Pantleon, Resolving the geometrically necessary dislocation content by conventional electron backscattering diffraction, Scr. Mater. 58 (2008) 994–997, https://doi.org/10.1016/J.SCRIPTAMAT.2008.01.050.
[37] J.W. Kysar, Y. Saito, M.S. Oztop, D. Lee, W.T. Huh, Experimental lower bounds on geometrically necessary dislocation density, Int. J. Plast. 26 (2010) 1097–1123, https://doi.org/10.1016/J.IJPLAS.2010.03.009.
[38] D. Juul Jensen, Growth rates and misorientation relationships between growing nuclei/grains and the surrounding deformed matrix during recrystallization, Acta Metall. Mater. 43 (1995) 4117–4129, https://doi.org/10.1016/0956-7151(95)00111-8.
[39] N. Moelans, B. Blanpain, P. Wollants, An introduction to phase-field modeling of microstructure evolution, CALPHAD: Comput. Coupling Phase Diagrams Thermochem. 32 (2008) 268–294, https://doi.org/10.1016/j.calphad.2007.11.003.
[40] J.A. Warren, R. Kobayashi, A.E. Lobkovsky, W.C. Carter, Extending phase field models of solidification to polycrystalline materials, Acta Mater. 51 (2003) 6035–6058.
[41] R.E. Reed-Hill, R. Abbaschian, R. Abbaschian, Physical metallurgy principles, Van Nostrand New York, 1973.
[42] H. Jazaeri, F.J. Humphreys, Quantifying recrystallization by electron backscatter diffraction, J. Microsc. 213 (2004) 241–246, https://doi.org/10.1111/j.0022-2720.2004.01296.x.
[43] G. Gottstein, D.A. Molodov, L.S. Shvindlerman, D.J. Srolovitz, M. Winning, Grain boundary migration: misorientation dependence, Curr. Opin. Solid State Mater. Sci. 5 (2001) 9–14, https://doi.org/10.1016/S1359-0286(00)00030-9.
[44] Y. Huang, F.J. Humphreys, Measurements of grain boundary mobility during recrystallization of a single-phase aluminium alloy, Acta Mater. 47 (1999) 2259–2268, https://doi.org/10.1016/S1359-6454(99)00062-2.
[45] R. Kobayashi, J.A. Warren, W.C. Carter, A continuum model of grain boundaries, Phys. D Nonlinear Phenom. 140 (2000) 141–150, https://doi.org/10.1016/S0167-2789(00)00023-3.
[46] D. Raabe, Scaling Monte Carlo kinetics of the Potts model using rate theory, Acta Mater. 48 (2000) 1617–1628, https://doi.org/10.1016/S1359-6454(99)00451-6.
[47] L. Madej, M. Sitko, K. Radwański, R. Kuziak, K. Radwanski, R. Kuziak, Validation and predictions of coupled finite element and cellular automata model: Influence of the degree of deformation on static recrystallization kinetics case study, Mater. Chem. Phys. 179 (2016) 282–294, https://doi.org/10.1016/j.matchemphys.2016.05.040.
[48] A.D.D. Rollett, D. Raabe, A hybrid model for mesoscopic simulation of recrystallization, Comput. Mater. Sci. 21 (2001) 69–78, https://doi.org/10.1016/S0927-0256(00)00216-0.
[49] K. Russell, Grain boundary nucleation kinetics, Acta Metall. 17 (1969) 1123–1131, https://doi.org/10.1016/0001-6160(69)90057-1.
[50] P.A. Beck, P.R. Sperry, C.S. Smith, J.E. Burke, P.R. Sperry, C.S. Smith, J.E. Burke, Strain induced grain boundary migration in high purity aluminum, J. Appl. Phys. 21 (1950) 150–152, https://doi.org/10.1063/1.1699614.
[51] P.A. Beck, The Formation of Recrystallization Nuclei, J. Appl. Phys. 20 (1949) 633–634, https://doi.org/10.1063/1.1698446.
[52] R.W. Cahn, A New Theory of Recrystallization Nuclei, Proc. Phys. Soc. Sect. A. 63 (1950) 323–336, https://doi.org/10.1088/0370-1298/63/4/302.